







The high-energy environment of the heavy sub-Earth GJ 367 b indicates likely complete evaporation of its atmosphere

K. Poppenhaeger^{1,2,*} , L. Ketzer^{1,2}, N. Ilic^{1,2} , E. Magaudda³, J. Robrade⁴ , B. Stelzer³ ,
J. H. M. M. Schmitt⁴ , and P. C. Schneider⁴ 

¹ Leibniz Institute for Astrophysics Potsdam (AIP), An der Sternwarte 16, 14482 Potsdam, Germany

² Institute for Physics and Astronomy, University of Potsdam, Karl-Liebknecht-Str. 24/25, 14476 Potsdam-Golm, Germany

³ Institut für Astronomie und Astrophysik (IAAT), Eberhard Karls Universität Tübingen, Sand 1, 72076 Tübingen, Germany

⁴ Hamburger Sternwarte, Gojenbergsweg 112, 21029 Hamburg, Germany

Received 26 January 2024 / Accepted 12 July 2024

ABSTRACT

The planet GJ 367 b is a recently discovered high-density sub-Earth orbiting an M dwarf star. Its composition was modelled to be predominantly iron with a potential remainder of a hydrogen-helium envelope. Here we report an X-ray detection of this planet's host star for the first time, using data from the spectro-imaging X-ray telescope eROSITA onboard the Spectrum-Roentgen-Gamma mission. We characterise the magnetic activity of the host star from the X-ray data and estimate its effects on a potential atmosphere of the planet. We find that despite the very low activity level of the host star the expected mass loss rates, both under core-powered and photoevaporative mass loss regimes, are so high that a potential primordial or outgassed atmosphere would evaporate very quickly. Since the activity level of the host star indicates that the system is several Giga-years old, it is very unlikely that the planet currently still hosts any atmosphere.

Key words. planets and satellites: atmospheres – stars: coronae – stars: low-mass – planetary systems – X-rays: individuals: GJ 367

1. Introduction

As exoplanet detection techniques have matured, planets in the Earth-sized regime have become detectable. Especially M dwarfs as host stars provide an advantage for the detection of small planets, since their small stellar radii yield sufficiently deep transits when a small rocky planet crosses the star. The planetary radius from transit observations can be combined with the planetary mass from radial velocity measurements to yield the planetary mean density, which in turn allows some inferences on the planetary composition.

Exoplanets that have radii similar to or smaller than Earth have been inferred to have a range of different compositions, with Trappist-1e (Grimm et al. 2018) and *f* (Agol et al. 2021) having similar densities to Earth and Venus, while other exoplanets have been found to display significantly lower densities which can be indicative of water envelopes (for example, Kepler-138b, Jontof-Hutter et al. 2015; Trappist-1h, Agol et al. 2021). The small exoplanet GJ 367b was discovered to have a surprisingly high density implying a high iron content (Lam et al. 2021). Modelling by the same authors showed that the planet can be described well if the planet is composed of iron for 90% of its interior, the remaining outer 10% consisting of a mantle layer and a small fraction of water ice VII (a specific crystalline form of ice) as well as hydrogen and helium in gaseous form. Recently, two additional planets at longer periods were found for the GJ 367 system through radial velocity observations, and planetary parameters for planet *b* were refined (Goffo et al. 2023).

Exoplanets have been found to undergo significant atmospheric evolution; one signpost of this is the so-called radius gap of small planets, an observed dearth of planets with radii around $2 R_{\oplus}$ (Fulton et al. 2017; Van Eylen et al. 2018). This is typically interpreted as planets losing their primordial hydrogen-helium envelopes through some process, where bare rocky planets live below the gap and the ones with significant hydrogen-helium envelopes remaining populate the parameter space above the gap. Different processes may be driving this atmospheric mass loss; two prominent scenarios are atmospheric escape driven by the internal heat of the planet (core-driven escape, Gupta & Schlichting 2020), and escape driven by the high-energy irradiation by the host star (see for example Murray-Clay et al. 2009; Owen & Wu 2017; Kubyschkina et al. 2018; Mordasini 2020), which can have a variety of different flavours depending on the assumptions made in the respective models.

Here we report on a first-time X-ray detection of GJ 367b's host star, which is an early M dwarf in the solar neighbourhood (see Table 1 for an overview of the system's properties). The detection was achieved using data from the eROSITA X-ray instrument (Section 2). This allows us to determine the coronal properties of the host star (Section 3) and to characterise the high-energy environment and possible evaporation rate of the exoplanet associated with irradiation (Section 4).

2. Observations and data analysis

eROSITA (Predehl et al. 2021) is an X-ray instrument onboard the Spectrum-Roentgen-Gamma spacecraft (Sunyaev et al. 2021). It was launched in July 2019 into an orbit around the L_2 Lagrange point of the Sun-Earth system. eROSITA consists of

* Corresponding author; kpoppenhaeger@aip.de

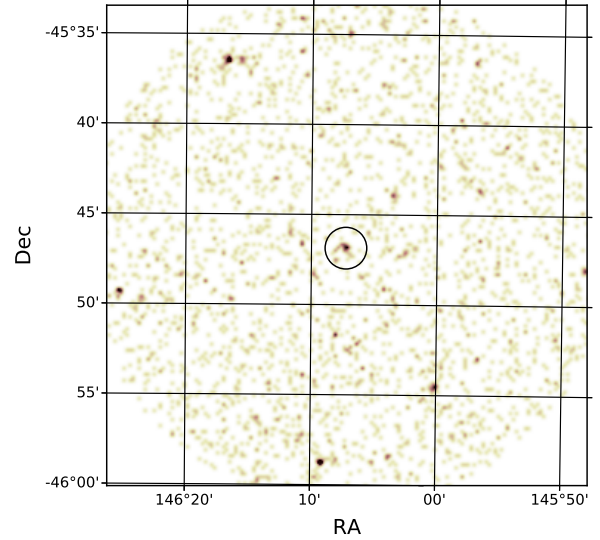
Table 1. Properties of the GJ 367 star-planet system from Lam et al. (2021).

Property	Value
stellar parameters:	
Spectral type	M1.0V
Mass	$0.454 M_{\odot}$
Radius	$0.457 R_{\odot}$
Distance	9.41 pc
Rotation period	48 ± 2 d
Planetary parameters:	
Mass	$0.55 M_{\oplus}$
Radius	$0.72 R_{\oplus}$
Semi-major axis	0.0071 AU
Orbital period	0.322 d

seven Wolter telescopes with one camera assembly each and is sensitive to photon energies between 0.2 and 10 keV. eROSITA started an all-sky survey in December 2019, where it scanned the whole sky every six months in great circles roughly perpendicular to the ecliptic. Any point on the sky is scanned every four hours for several eROSITA slews, with the number of slews when a given target is in the field of view depending on the ecliptic latitude of the target.

eROSITA has completed four all-sky surveys to date (named eRASS1 to eRASS4). We accessed the data around GJ 367's position in the form of photon event files for each of the four surveys, and additionally used the source catalogues produced by the consortium. Specifically, we used the stacked source catalogue in the current data reduction version from October 31 2022, as released to the eROSITA-DE consortium¹. For the photon event files we used the data processing version 020 of eROSITA-DE. The eROSITA source catalogue was constructed by performing a source detection on the stacked X-ray images from the first four eRASS surveys in the 0.2–2.3 keV band, and then using the identified source positions to perform forced photometry in narrower energy bands; this stacked catalogue is referred to as eRASS:4. For an overview of the data reduction software for eROSITA see Brunner et al. (2022), and for an overview of the data release of the eRASS1 data see the paper by Merloni et al. (2024).

We performed a separation-based cross-match of the eRASS:4 catalogue to the optical position of GJ 367 as identified in the *Gaia* DR3 catalogue (Gaia Collaboration 2023). GJ 367 has a significant proper motion of about 0.7 arcsec per year, and it was observed by eROSITA about half-yearly from June 2020 to December 2021. Therefore we chose the star's position at the epoch of March 31 2021 as its representative mean position for the relevant eROSITA scanning period, yielding coordinates of RA = 09:44:28.897 and Dec = -45:46:47.808. We cross-matched this optical position of GJ 367 with the eRASS:4 catalogue and found an X-ray source within an on-sky separation of 6'', which is within two sigma of the typical positional uncertainty of eROSITA (Brunner et al. 2022); we therefore identify this X-ray source with GJ 367. The effective exposure time at GJ 367's position is about 600 s. Since eROSITA surveys scan the sky on great-circles, the effective exposure time of a sky location varies slightly for different photon energies due to


Fig. 1. Combined X-ray image from the first four eRASS surveys around the position of GJ 367, indicated by the circle, in the soft eROSITA X-ray band (0.2–2.3 keV). GJ 367 displays a clear excess in X-ray photons compared to the ambient background.

energy-dependent vignetting effects, but this variation is small for the soft X-ray energies at which GJ 367 emits.

3. Results

3.1. X-ray upper limits from previous observations

In the past the position of the GJ 367 system was observed by the ROSAT All-Sky Survey (Boller et al. 2016) and multiple times with the XMM-Newton Slew Survey (Saxton et al. 2008; Freund et al. 2018), both of which yielded unrestrictive upper limits to the X-ray flux of the star. We calculated the corresponding upper limits with the XMM-Newton Upper Limit Server² to be $F_{X,ROSAT} \leq 2.79 \times 10^{-13} \text{ erg s}^{-1} \text{ cm}^{-2}$ from ROSAT and the strictest of the XMM-Newton Slew Survey upper limits to be $F_{X,XMM\text{sllew}} \leq 6.33 \times 10^{-13} \text{ erg s}^{-1} \text{ cm}^{-2}$. With a distance of 9.41 pc this corresponds to an upper limit to the X-ray luminosity of the star of $L_{X,ROSAT} \leq 3.0 \times 10^{27} \text{ erg s}^{-1}$.

3.2. X-ray properties from eROSITA

The combined signal from the four completed eRASS scans of GJ 367's position clearly displays an X-ray excess; we show the combined soft X-ray image produced from the photon event files in the 0.2–2.3 keV energy band in Fig. 1. In the eRASS:4 source catalogue, the source we identified with GJ 367 is significantly detected. The detection significance is determined in the eROSITA data reduction as the negative logarithm of the probability that the observed excess counts have arisen as a chance fluctuation of the background, meaning that larger log-likelihood values correspond to more significant source detections. A minimum log-likelihood threshold of 5 was applied in the construction of the catalogue; GJ 367 has a log-likelihood value of 32 for the 0.2–2.3 keV energy band, making it a solid detection.

3.2.1. Stellar coronal temperature

The ROSAT non-detection of GJ 367 implies that it has a moderate to low X-ray luminosity for an M dwarf, which we discuss

¹ The consortium-internal catalogue file name that was used was all_s4_SourceCat1B_221031_poscorr_mpe_photom.fits.

² <http://xmmuls.esac.esa.int/upperlimitserver/>

Table 2. X-ray net source count rates, hardness ratios and coronal X-ray fluxes of GJ 367 in the combined first four eROSITA surveys for several energy bands³.

Energy band	Count rate (cts s ⁻¹)	Hardness ratio	X-ray flux (erg s ⁻¹ cm ⁻²)
narrow eROSITA bands:			
0.2–0.5 keV	0.018 ± 0.006	HR ₁₂ = 0.06 ± 0.23	(2.64 ± 0.88) × 10 ⁻¹⁴
0.5–1.0 keV	0.020 ± 0.007	–	(1.57 ± 0.53) × 10 ⁻¹⁴
1.0–2.0 keV	≤0.005	–	<0.42 × 10 ⁻¹⁴
broad eROSITA soft band:			
0.2–2.3 keV	0.041 ± 0.010	–	(4.71 ± 1.08) × 10 ⁻¹⁴

in more detail in Section 4.1. The star can therefore be expected to have a soft X-ray spectrum, as X-ray luminosity and temperature are correlated for stellar coronal spectra (see for example Schmitt 1997; Johnstone & Güdel 2015; Magaúda et al. 2022).

Since the determination of X-ray fluxes and luminosity depends on the underlying spectral shape, we proceeded by estimating the coronal temperature for GJ 367 from the collected eROSITA data.

A total of 24.9 source counts above the background were collected in the 0.2–2.3 keV band; this is a maximum-likelihood estimate for the source counts that takes into account vignetting and the local background and is therefore not an integer number. This number of collected counts is small and allows only a low signal-to-noise (S/N) spectrum to be extracted. We therefore first considered the hardness ratio of the two softest bands of the star, with $HR_{12} = (R_2 - R_1)/(R_2 + R_1)$ where R_2 is the excess count rate in the harder band and R_1 in the softer band, and energy bands of 0.2–0.5 and 0.5–1.0 keV were chosen. The hardness ratio from the catalogue photon counts is listed in Table 2 as well, with $HR_{12} = 0.06 \pm 0.23$.

To convert this into an estimate for the typical coronal temperature of GJ 367, we used the same methodology as used in other works (Poppenhäger et al. 2009; Foster et al. 2022), i.e. we simulated coronal spectra over the instrumental spectral response and calculated the resulting hardness ratios as a function of coronal temperature. Specifically, we employed an optically thin thermal plasma model as appropriate for a stellar corona, and used the Xspec spectral fitting software (Arnaud 1996) and its implemented APEC spectral model (Smith et al. 2001; Foster et al. 2012) to simulate spectra on a fixed temperature grid. We show the hardness ratios for the relevant spectral bands derived from the simulated spectra in Fig. 2, together with the measured hardness ratios for GJ 367. We found that the observed hardness ratios are in agreement with a coronal temperature in the range of 0.16 ± 0.03 keV, corresponding to about 1.82 ± 0.34 MK. We point out here the same caveat already mentioned by Foster et al. (2022), that the relationship between the hardness ratio and the coronal temperature is well-defined for stellar coronae with a single dominant temperature component, but may not represent coronae well in which two or more disparate strong temperature components are present.

3.2.2. Stellar X-ray luminosity

The eROSITA source catalogues present source fluxes derived from count rates by assuming an underlying absorbed power-law

³ The values are given with 1σ uncertainties; the upper limit in the 1.0–2.0 keV band is given as the one-sided 90% confidence range, calculated as described in Tubín-Arenas et al. (2024).

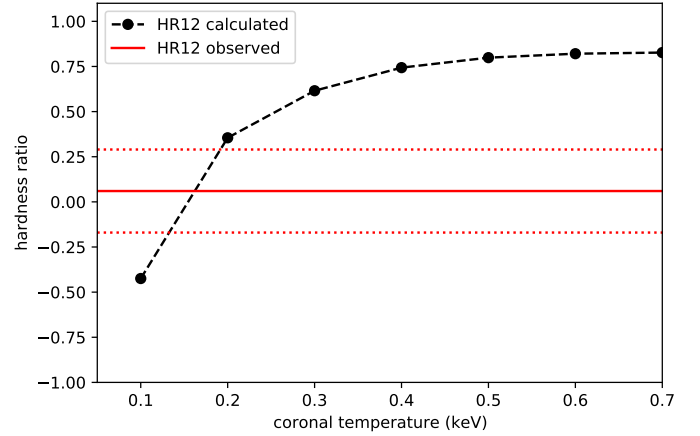


Fig. 2. Measured X-ray hardness ratio HR₁₂ of GJ 367 (red solid line, with red dotted lines indicating 1σ uncertainties) compared to the same hardness ratio for simulated X-ray spectra of different coronal temperatures (black dots and dashed line). GJ 367's hardness ratio implies a mean coronal temperature in the 0.13–0.19 keV range, i.e. about 1.5–2.2 million K.

spectrum as specified in Brunner et al. (2022). In contrast, X-ray emission from stellar coronae is described by an optically thin thermal plasma instead of a power law, which yields different conversion factors between count rates and X-ray fluxes.

We therefore determined flux conversion factors that are appropriate for an underlying coronal spectrum with a temperature of 1.82 MK, instead of an underlying power-law spectrum. This procedure is described in detail in Tubín-Arenas et al. (2024); in short, one simulates an absorbed power-law spectrum and the appropriate coronal spectrum over the eROSITA instrumental response and effective area, which are taken from the eROSITA Calibration Database, and calculates the resulting flux conversion factors. Using this approach, we found the following appropriate flux conversion factors (*ecfs*) for GJ 367's coronal temperature for the energy bands we are interested in, which yield the coronal fluxes when multiplying with the count rate for each band:

$$\begin{aligned}
 ecf_{\text{cor}, 0.2-0.5 \text{ keV}} &= 1.49 \times 10^{-12} \text{ erg s}^{-1} \text{ cm}^{-2} \text{ count}^{-1}, \\
 ecf_{\text{cor}, 0.5-1 \text{ keV}} &= 0.79 \times 10^{-12} \text{ erg s}^{-1} \text{ cm}^{-2} \text{ count}^{-1}, \\
 ecf_{\text{cor}, 1-2 \text{ keV}} &= 0.85 \times 10^{-12} \text{ erg s}^{-1} \text{ cm}^{-2} \text{ count}^{-1}, \\
 ecf_{\text{cor}, 0.2-2.3 \text{ keV}} &= 1.14 \times 10^{-12} \text{ erg s}^{-1} \text{ cm}^{-2} \text{ count}^{-1},
 \end{aligned}$$

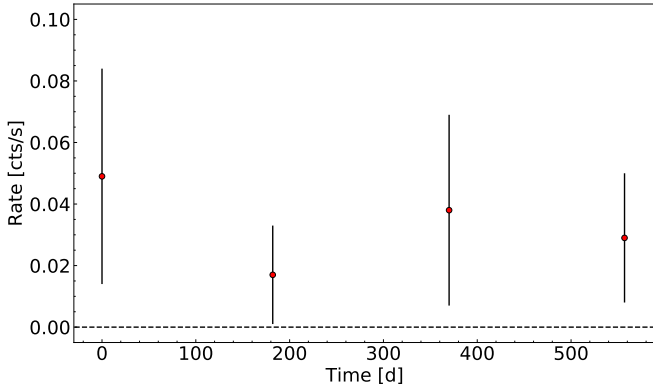
Applying these conversion factors yielded stellar X-ray fluxes for GJ 367 as listed in Table 2. Unsurprisingly for such a cool corona, the emission is very soft, and within narrow energy bands, the source is only individually detected in the 0.2–0.5 keV and 0.5–1.0 keV band. The 1.0–2.0 keV band showed a weak excess, yielding no significant detection in that band alone. The standard eROSITA energy band of 0.2–2.3 keV yielded a total coronal flux, using the correction factor for that band, of $(4.71 \pm 1.08) \times 10^{-14} \text{ erg s}^{-1} \text{ cm}^{-2}$. We used this value for the following luminosity and surface flux calculation of GJ 367.

We derived an X-ray luminosity of $(5.0 \pm 1.1) \times 10^{26} \text{ erg s}^{-1}$ in the 0.2–2.3 keV energy band, using the stellar distance of 9.41 pc as listed in Table 1. The detected X-ray luminosity of the host star is, therefore, fainter than the previous ROSAT upper limit by a factor of about six.

Other relevant properties that can be calculated from the stellar X-ray luminosity are the stellar activity indicator $\log(L_X/L_{\text{bol}})$

Table 3. Derived X-ray properties of the exoplanet host star GJ 367.

X-ray property (0.2–2.3 keV band)	Value
X-ray luminosity L_X	$(5.0 \pm 1.1) \times 10^{26} \text{ erg s}^{-1}$
Mean coronal temperature T_{cor}	$1.82 \pm 0.34 \text{ MK}$
Activity indicator $\log(L_X/L_{\text{bol}})$	$-5.34^{+0.09}_{-0.11}$
X-ray flux through stellar surface $F_{X,\text{surf}}$	$(3.9 \pm 0.9) \times 10^4 \text{ erg s}^{-1} \text{ cm}^{-2}$
X-ray flux at planetary orbit $F_{X,\text{pl}}$	$3.5 \times 10^3 \text{ erg s}^{-1} \text{ cm}^{-2}$


Fig. 3. X-ray light curve of GJ 367 over the four half-yearly eRASS surveys, displayed as source count rates in the 0.2–2.3 keV band with 1σ uncertainties.

and the X-ray flux through the stellar photospheric surface $F_{X,\text{surf}} = L_X/(4\pi R_*^2)$. We estimated the stellar bolometric luminosity from the color relations given by Mann et al. (2015, 2016), which yielded $L_{\text{bol}} = 0.030 L_{\text{bol},\odot} = 1.1 \times 10^{32} \text{ erg s}^{-1}$. The activity indicator then works out to $\log(L_X/L_{\text{bol}}) = -5.34^{+0.09}_{-0.11}$ and the flux through the stellar surface to $F_{X,\text{surf}} = (3.9 \pm 0.9) \times 10^4 \text{ erg s}^{-1} \text{ cm}^{-2}$. We list all relevant X-ray quantities together in Table 3.

3.2.3. X-ray variability

GJ 367 does not display any strong variability in the data collected by eRASS1:4 surveys. We show the detected mean count rates per eRASS survey in Fig. 3. They display mild variability within a factor of two, but this is consistent with a constant source flux within the uncertainties of the measurements.

4. Discussion

4.1. The present-day magnetic activity environment of GJ 367 b

The derived X-ray properties of GJ 367 mark it as an M dwarf with very low activity. In the context of older surveys of M dwarf X-ray luminosities, such as the sample collected by Schmitt et al. (1995) with ROSAT, it does not seem to be remarkably low in X-ray luminosity. However, this is due to the fact that GJ 367 sits at the high end of the mass and radius range of M dwarfs. The X-ray luminosity is therefore not the most suitable activity indicator to compare the star to other M dwarfs; rather, the fractional X-ray luminosity $R_X = \log(L_X/L_{\text{bol}})$ is of interest, which normalises for the large size and effective temperature range present in M dwarfs of different masses. This is demonstrated by more recently analyzed X-ray samples of M dwarfs (Magaudda et al. 2022; Caramazza et al. 2023), where GJ 367 does actually sit

at the lower end of observed fractional X-ray luminosities with respect to the M dwarfs that occupy a similar mass range to GJ 367.

The fractional X-ray luminosity R_X can be put into context with the stellar rotation period. All reported rotation periods for GJ 367 are quite long: Lam et al. (2021) report a period of 48 ± 2 days from flux modulation in broad-band light curves; estimates for the rotation period derived from chromospheric activity indicators are in the range of 54 to 58 days (Lam et al. 2021; Goffo et al. 2023); and an analysis of variations in observed radial velocities yielded a period estimate of 51.30 ± 0.13 days (Goffo et al. 2023). We use here the value of 48 days derived from light curve modulation, but we point out that using one of the other values does not make any significant difference in the following discussion. We calculated GJ 367’s Rossby number $Ro = P_{\text{rot}}/\tau_{\text{conv}} = 0.93$ using the rotation period P_{rot} from Lam et al. (2021) and estimated the convective turnover time τ_{conv} from the relation determined by Wright et al. (2018). We derived the fractional X-ray luminosity $R_X = -5.34$ in Sect. 3.2.2. We compare this to the sample presented by Magaudda et al. (2022), highlighting the M dwarfs with masses between 0.4 and $0.6 M_{\odot}$ in turquoise (see Fig. 4). Here we see that GJ 367 falls into the slowly-rotating, low-activity tail of the distribution. It is among the lowest-activity M dwarfs with measured rotation periods, but not an outlier in terms of the overall rotation-activity relation. Together with its long rotation period (see Table 1), the low X-ray activity suggests a mature main-sequence age of the star of several Gyr (see for example Gruner et al. 2023; Curtis et al. 2020).

While the stellar coronal temperature and absolute X-ray luminosity are on the low end compared to other M dwarfs, the high-energy environment of the exoplanet GJ 367 b is intense nevertheless, since the planet is located at a distance of only 0.0071 AU to the host star. We calculate the high-energy flux the planet receives in its orbit from the planetary orbital parameters derived by Lam et al. (2021), which are also listed in Table 1. We find an X-ray flux at the planetary orbit of $F_{X,\text{pl}} = 3.5 \times 10^3 \text{ erg s}^{-1} \text{ cm}^{-2}$ in the 0.2–2.3 keV band. This is lower by only about a factor of two than the X-ray irradiation of the evaporating hot Jupiter HD 189733 b (Poppenhaeger et al. 2013; Pillitteri et al. 2014).

4.2. Stellar activity effects on any remaining atmosphere of the planet

Modelling of the planet GJ 367 b presented by Lam et al. (2021) suggests a core consisting predominantly of iron surrounded by a mantle, with the possibility of a thin hydrogen-helium atmosphere on top. How much of an atmosphere is to be expected from those models depends on the density of the planet. Lam et al. (2021) modelled the mass budget for the atmosphere to be up to 1% of the planetary mass for their reported most probable density of 8.106 g cm^{-3} , and significantly smaller for higher densities of around 10 g cm^{-3} , as were reported by Goffo et al. (2023). Whether very small and hot exoplanets such as GJ 367 b actually form with a primordial hydrogen-helium envelope at all is currently unclear (Neil & Rogers 2020; Qian & Wu 2021); however, even if no primordial hydrogen-helium envelope is present, volatiles in the magma of young rocky planets may lead to outgassing and a hydrogen-dominated atmosphere (Katyal et al. 2020). Finally, heavier outgassed atmospheres have been discussed for GJ 367 b (Zhang et al. 2024).

We therefore briefly discuss the stability of a potential atmosphere of GJ 367 b under different scenarios. Two different mass

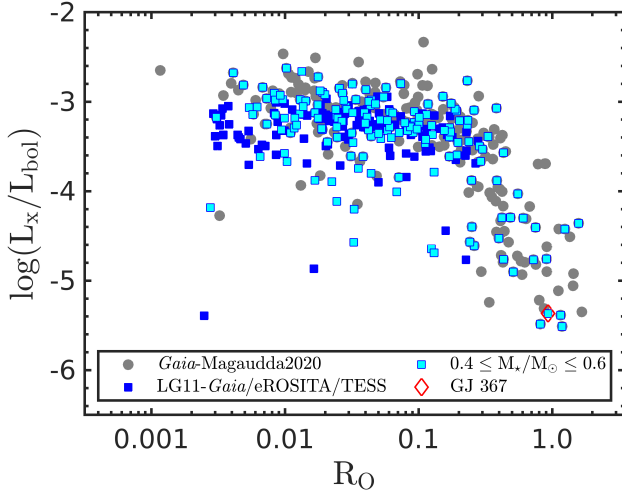


Fig. 4. GJ 367’s X-ray activity in the context of other M dwarfs in the same mass range (from Magaudda et al. 2022) as a function of the Rossby number. GJ 367 falls into the low-activity tail of the distribution and is one of the lowest-activity M dwarfs with detected X-ray emission and rotation period; however, it is not unusually X-ray inactive compared to other M dwarfs at large Rossby numbers.

loss drivers are considered to be most important for close-in exoplanets: core-powered mass loss driven by planetary internal heat (Ginzburg et al. 2018; Gupta & Schlichting 2019); and photoevaporation driven by stellar high-energy irradiation (Watson et al. 1981; Murray-Clay et al. 2009). An analytical approximation for photoevaporation is the energy-limited escape scenario, where the mass loss rate scales linearly with the stellar high-energy irradiation (Yelle 2004; Lecavelier des Etangs et al. 2004; Erkaev et al. 2007); for exoplanets with a weakly bound atmospheres, i.e. typically hot, close-in, and low-mass planets, hydrodynamic aspects are expected to cause much stronger mass loss rates than predicted by the energy-limited approximation (Kubyschkina et al. 2018; Koskinen et al. 2022). A useful parameter to distinguish between the different mass-loss regimes is the Jeans parameter, defined as

$$\Lambda = \frac{GM_{\text{pl}}\mu_{\text{atm}}}{k_{\text{B}}R_{\text{pl}}T_{\text{eq}}}, \quad (1)$$

where G is the gravitational constant, M_{pl} the planetary mass, μ_{atm} the mean molecular mass of the escaping atmosphere, k_{B} the Boltzmann constant, R_{pl} the planetary radius, and T_{eq} the planetary equilibrium temperature (Fossati et al. 2017, see also Guo 2024). Photo-evaporation of atmospheres in the energy-limited regime is expected to become the dominant mass loss mechanism at large $\Lambda \gtrsim 10$ (Kubyschkina & Fossati 2021; Fernández Fernández et al. 2023).

For $\Lambda < 10$, i.e. for low-mass and hot planets, core-powered escape quickly becomes dominant. In the case of GJ 367 b, $\Lambda = 6.3$ for a hydrogen-helium atmosphere. Typical mass loss rates in this Λ regime have been modelled to be of the order of 10^{15} – 10^{18} g s^{-1} (Kubyschkina & Fossati 2021). Even if we assume that GJ 367 b currently holds a hydrogen-helium atmosphere amounting to 1% of its planetary mass (i.e. as modelled by Lam et al. 2021), this atmospheric mass would amount to ca. 3×10^{27} g and would be lost within about 0.1 Myr even at the lower end of those typical mass loss rates. So, given the low magnetic activity of the host star and its expected age of

several Gigayears, no hydrogen-helium atmosphere is expected to be currently present for GJ 367 b.

However, heavier atmospheres that may have been outgassed by the hot mantle of GJ 367 b, such as a carbon dioxide dominated atmosphere, have been discussed in the literature as well (Zhang et al. 2024). For a carbon dioxide dominated atmosphere, GJ 367 b’s Λ would be 53, which would place the planet in the energy-limited escape regime. We therefore estimate the X-ray and extreme-UV (together, XUV) irradiation of the planet in the following, which is the main driver of energy-limited atmospheric escape. We do point out as a caveat that the typical efficiency factors of energy-limited escape have only been modelled for hydrogen-helium atmospheres, while a much larger fraction of the incoming stellar XUV flux may drive photochemistry in heavier atmospheres and therefore not be available to drive an efficient evaporation process. So, any estimates of the energy-limited mass loss rates will be severely limited by this lacking knowledge. Following our calculation of the stellar XUV irradiation of the planet, we will therefore only briefly comment on possible escape rates.

While the X-ray luminosity is known thanks to eROSITA, the extreme-UV (EUV) emission of the host star needs to be estimated, since no observatories are currently operating in the EUV regime. EUV photons are the main contributor to the photoionization of hydrogen, which in turn can cause heating and mass loss from the planetary atmosphere (e.g. Watson et al. 1981; Murray-Clay et al. 2009).

We use two empirical scaling relationships to obtain a general estimate of the EUV flux. One of them calculates the EUV flux based on an X-ray and EUV surface flux scaling relation (Johnstone et al. 2021), while the other scales X-ray and EUV energy bands for late-type stars based on synthetic XUV spectra (Sanz-Forcada et al. 2011). Both use an input X-ray band of 0.1–2.4 keV and calculate EUV fluxes for a band of 0.013 to 0.1 keV (equalling 100–920 Å). We estimate GJ 367’s X-ray luminosity in the 0.1–2.4 keV band to be 5.7×10^{26} erg s^{-1} , using its measured luminosity in the 0.2–2.3 keV band and coronal temperature of 1.82 MK in the WebPIMMS tool⁴. We then obtain $L_{\text{EUV}} = 2.8 \times 10^{27}$ erg s^{-1} and $L_{\text{EUV}} = 6.4 \times 10^{27}$ erg s^{-1} for the surface flux and synthetic spectra relations, respectively. This leads to a combined X-ray and EUV (XUV) luminosity of $L_{\text{XUV}} = 3.3 \times 10^{27}$ erg s^{-1} for the surface flux relation, and $L_{\text{XUV}} = 7.0 \times 10^{27}$ erg s^{-1} for the synthetic spectra relation. For GJ 367, the EUV flux is relatively well constrained, with both estimates agreeing within a factor of two. We do not make use of the Linsky et al. (2014) X-ray to Ly α relation due to its applicability to K-F spectral types, only. Averaging between both estimates, we find an XUV irradiation flux that GJ 367 b receives from its host star that amounts to 3.65×10^4 $\text{erg s}^{-1} \text{cm}^{-2}$.

Keeping in mind the caveat mentioned above that efficiency factors for energy-limited escape may be very small for heavy atmospheres, we take a brief look at possible escape rates. The energy-limited mass loss rate of planets can be estimated as (Erkaev et al. 2007, see also Owen & Jackson 2012):

$$\dot{M}_{\text{en-lim}} = -\epsilon \frac{(\pi R_{\text{XUV}}^2) F_{\text{XUV}}}{KGM_{\text{pl}}/R_{\text{pl}}} = -\epsilon \frac{3\beta^2 F_{\text{XUV}}}{4GK\rho_{\text{pl}}}. \quad (2)$$

Here, M_{pl} and ρ_{pl} are the mass and density of the planet, R_{pl} and R_{XUV} the planetary radii at optical and XUV wavelengths, with $R_{\text{XUV}} \approx R_{\text{pl}}$ assumed for a heavy atmosphere. Impacts of

⁴ <https://heasarc.gsfc.nasa.gov/cgi-bin/Tools/w3pimms/w3pimms.pl>

Roche lobe overflow (Erkaev et al. 2007) are encompassed in the factor K , which can take on values of 1 for no Roche lobe influence and <1 for planets filling significant fractions of their Roche lobes; in the case of GJ 367 b, we calculate a Roche lobe radius of 2.5 times the optical planetary radius and find a corresponding value of $K = 0.43$ from the system parameters as given by Lam et al. (2021). The high-energy XUV flux received by the planet is given by F_{XUV} , and the efficiency of the atmospheric escape by ϵ . The efficiency ϵ is highly uncertain; for hydrogen-helium atmospheres, they have been modelled to be on the order of 10 to 30% where the energy-limited approximation applies (see e.g. Owen & Wu 2013; Salz et al. 2016). Assuming ad hoc an efficiency that is an order of magnitude lower ($\epsilon = 0.01$) for a carbon dioxide dominated atmosphere, the mass loss rate would work out to about 10^9 g/s. Zhang et al. (2024) determined a maximum amount of carbon dioxide dominated atmosphere of 1 bar from a lack of an atmospheric detection in JWST observations of GJ 367 b. This translates to an atmospheric mass of ca. 2.5×10^{21} g. With the mass loss rate stipulated above, this atmosphere would be fully evaporated in less than 0.1 Myr.

As we have discussed above, the X-ray luminosity and spectral hardness of the host star suggest that the system is several Gigayears old, in line with the long rotation period derived by Lam et al. (2021). Therefore, it is statistically very unlikely that the planet currently still hosts an atmosphere, when its density can also be modelled by an atmosphere-free iron-dominated rock. Our findings are consistent with the recently obtained upper limit on a present atmosphere of GJ 367 b from mid-infrared JWST observations (Zhang et al. 2024).

Nevertheless, small rocky planets such as GJ 367 b are interesting laboratories to improve our understanding of atmosphere survival. The specific case of this exoplanet shows that even low-activity M dwarfs can drive significant mass loss rates in the most compact systems.

5. Conclusions

We have presented the first X-ray detection of GJ 367, an M dwarf star hosting a recently discovered, extremely dense mini-Earth. We characterise the host star to have a low-temperature corona and an X-ray luminosity typical for old, inactive M dwarfs in the solar neighbourhood. Due to its proximity to the host star, a potentially present primary or outgassed atmosphere is vulnerable to mass loss. We find that a primordial hydrogen-helium atmosphere would be very quickly lost under the core-powered mass loss regime, and a heavier outgassed atmosphere can be expected to become evaporated by the stellar high-energy flux on short time scales as well. Therefore, it is unlikely that this planet currently hosts any remainders of an atmosphere.

Acknowledgements. The authors thank the anonymous referee for their insightful comments. K.P., N.I., and L.K. acknowledge support from the German Leibniz-Gemeinschaft under project number P67/2018. E.M. is supported by Deutsche Forschungsgemeinschaft under grant STE 1068/8-1. J.R. acknowledges support from the DLR under grant 50QR2105 and PCS from DLR grant 50OR2102. This work is based on data from eROSITA, the soft X-ray instrument aboard SRG, a joint Russian-German science mission supported by the Russian Space Agency (Roskosmos), in the interests of the Russian Academy of Sciences represented by its Space Research Institute (IKI), and the Deutsches Zentrum für Luft- und Raumfahrt (DLR). The SRG spacecraft was built by Lavochkin Association (NPOL) and its subcontractors, and is operated by NPOL with support from the Max Planck Institute for Extraterrestrial Physics (MPE). The development and construction of the eROSITA X-ray instrument was led by MPE, with contributions from the Dr. Karl Remeis Observatory Bamberg & ECAP (FAU Erlangen-Nuernberg), the University of Hamburg Observatory, the Leibniz Institute for Astrophysics Potsdam (AIP), and the Institute for Astronomy

and Astrophysics of the University of Tübingen, with the support of DLR and the Max Planck Society. The Argelander Institute for Astronomy of the University of Bonn and the Ludwig Maximilians Universität Munich also participated in the science preparation for eROSITA.

References

- Agol, E., Dorn, C., Grimm, S. L., et al. 2021, *Planet. Sci. J.*, 2, 1
 Arnaud, K. A. 1996, *ASP Conf. Ser.*, 101, 17
 Boller, T., Freyberg, M. J., Trümper, J., et al. 2016, *A&A*, 588, A103
 Brunner, H., Liu, T., Lamer, G., et al. 2022, *A&A*, 661, A1
 Caramazza, M., Stelzer, B., Magaudda, E., et al. 2023, *A&A*, 676, A14
 Curtis, J. L., Agüeros, M. A., Matt, S. P., et al. 2020, *ApJ*, 904, 140
 Erkaev, N. V., Kulikov, Y. N., Lammer, H., et al. 2007, *A&A*, 472, 329
 Fernández Fernández, J., Wheatley, P. J., & King, G. W. 2023, *MNRAS*, 522, 4251
 Fossati, L., Erkaev, N. V., Lammer, H., et al. 2017, *A&A*, 598, A90
 Foster, A. R., Ji, L., Smith, R. K., & Brickhouse, N. S. 2012, *ApJ*, 756, 128
 Foster, G., Poppenhaeger, K., Ilic, N., & Schwöpe, A. 2022, *A&A*, 661, A23
 Freund, S., Robrade, J., Schneider, P. C., & Schmitt, J. H. M. M. 2018, *A&A*, 614, A125
 Fulton, B. J., Petigura, E. A., Howard, A. W., et al. 2017, *AJ*, 154, 109
 Gaia Collaboration (Vallenari, A., et al.) 2023, *A&A*, 674, A1
 Ginzburg, S., Schlichting, H. E., & Sari, R. 2018, *MNRAS*, 476, 759
 Goffo, E., Gandolfi, D., Egger, J. A., et al. 2023, *ApJ*, 955, L3
 Grimm, S. L., Demory, B.-O., Gillon, M., et al. 2018, *A&A*, 613, A68
 Gruner, D., Barnes, S. A., & Weingrill, J. 2023, *A&A*, 672, A159
 Guo, J. H. 2024, *Nat. Astron.*, in press
 Gupta, A., & Schlichting, H. E. 2019, *MNRAS*, 487, 24
 Gupta, A., & Schlichting, H. E. 2020, *MNRAS*, 493, 792
 Johnstone, C. P., & Güdel, M. 2015, *A&A*, 578, A129
 Johnstone, C. P., Bartel, M., & Güdel, M. 2021, *A&A*, 649, A96
 Jontof-Hutter, D., Rowe, J. F., Lissauer, J. J., Fabrycky, D. C., & Ford, E. B. 2015, *Nature*, 522, 321
 Katyal, N., Ortenzi, G., Lee Grenfell, J., et al. 2020, *A&A*, 643, A81
 Koskinen, T. T., Lavvas, P., Huang, C., et al. 2022, *ApJ*, 929, 52
 Kubyschkina, D. I., & Fossati, L. 2021, *Res. Notes Am. Astron. Soc.*, 5, 74
 Kubyschkina, D., Fossati, L., Erkaev, N. V., et al. 2018, *ApJ*, 866, L18
 Lam, K. W. F., Csizmadia, S., Astudillo-Defru, N., et al. 2021, *Science*, 374, 1271
 Lecavelier des Etangs, A., Vidal-Madjar, A., McConnell, J. C., & Hébrard, G. 2004, *A&A*, 418, L1
 Linsky, J. L., France, K., & Ayres, T. 2014, *IAU Symp.*, 293, 309
 Magaudda, E., Stelzer, B., Raetz, S., et al. 2022, *A&A*, 661, A29
 Mann, A. W., Feiden, G. A., Gaidos, E., Boyajian, T., & von Braun, K. 2015, *ApJ*, 804, 64
 Mann, A. W., Feiden, G. A., Gaidos, E., Boyajian, T., & von Braun, K. 2016, *ApJ*, 819, 87
 Merloni, A., Lamer, G., Liu, T., et al. 2024, *A&A*, 682, A34
 Mordasini, C. 2020, *A&A*, 638, A52
 Murray-Clay, R. A., Chiang, E. I., & Murray, N. 2009, *ApJ*, 693, 23
 Neil, A. R., & Rogers, L. A. 2020, *ApJ*, 891, 12
 Owen, J. E., & Jackson, A. P. 2012, *MNRAS*, 425, 2931
 Owen, J. E., & Wu, Y. 2013, *ApJ*, 775, 105
 Owen, J. E., & Wu, Y. 2017, *ApJ*, 847, 29
 Pillitteri, I., Wolk, S. J., Lopez-Santiago, J., et al. 2014, *ApJ*, 785, 145
 Poppenhaeger, K., Robrade, J., Schmitt, J. H. M. M., & Hall, J. C. 2009, *A&A*, 508, 1417
 Poppenhaeger, K., Schmitt, J. H. M. M., & Wolk, S. J. 2013, *ApJ*, 773, 62
 Predehl, P., Andritschke, R., Arefiev, V., et al. 2021, *A&A*, 647, A1
 Qian, Y., & Wu, Y. 2021, *AJ*, 161, 201
 Salz, M., Schneider, P. C., Czesla, S., & Schmitt, J. H. M. M. 2016, *A&A*, 585, L2
 Sanz-Forcada, J., Micela, G., Ribas, I., et al. 2011, *A&A*, 532, A6
 Saxton, R. D., Read, A. M., Esquej, P., et al. 2008, *A&A*, 480, 611
 Schmitt, J. H. M. M. 1997, *A&A*, 318, 215
 Schmitt, J. H. M. M., Fleming, T. A., & Giampapa, M. S. 1995, *ApJ*, 450, 392
 Smith, R. K., Brickhouse, N. S., Liedahl, D. A., & Raymond, J. C. 2001, *ApJ*, 556, L91
 Sunyaev, R., Arefiev, V., Babyshkin, V., et al. 2021, *A&A*, 656, A132
 Tubín-Arenas, D., Krumpke, M., Lamer, G., et al. 2024, *A&A*, 682, A35
 Van Eylen, V., Agentoft, C., Lundkvist, M. S., et al. 2018, *MNRAS*, 479, 4786
 Watson, A. J., Donahue, T. M., & Walker, J. C. G. 1981, *Icarus*, 48, 150
 Wright, N. J., Newton, E. R., Williams, P. K. G., Drake, J. J., & Yadav, R. K. 2018, *MNRAS*, 479, 2351
 Yelle, R. V. 2004, *Icarus*, 170, 167
 Zhang, M., Hu, R., Inglis, J., et al. 2024, *ApJ*, 961, L44